Journal Name

ARTICLE

Combining Magnetic Hyperthermia and dual *T1/T2* MR Imaging Using Highly Versatile Iron Oxide Nanoparticles

Received 00th January 20xx,
Accepted 00th January 20xx

DOI: 10.1039/x0xx00000x

www.rsc.org/

Santiago Sánchez-Cabezas,[a]* Roberto Montes-Robles,[a] Juan Gallo,[c] Félix Sancenón[a,b] and Ramón Martínez-Máñez[a,b]*

Magnetic hyperthermia and magnetic resonance imaging (MRI) are two of the most important biomedical applications of magnetic nanoparticles (MNPs). However, the design of MNPs with good heating performance for hyperthermia and dual *T1/T2* contrast for MRI remains a considerable challenge. In this work, ultrasmall superparamagnetic iron oxide nanoparticles (USPIONs) are synthesized through a simple one-step methodology. A post-synthetic purification strategy has been implemented in order to separate discrete nanoparticles from aggregates and unstable nanoparticles, leading to USPIONs that preserve chemical and colloidal stability for extended periods of time. The optimized nanoparticles exhibit high saturation magnetization and show good heating efficiency in magnetic hyperthermia experiments. Remarkably, the evaluation of the USPIONs as MRI contrast agents revealed that the nanoparticles are also able to provide significant dual *T1/T2* signal enhancement. These promising results demonstrate that USPIONs are excellent candidates for the development of theranostic nanodevices with potential application in both hyperthermia and dual *T1/T2* MR imaging.

Introduction

Magnetic nanoparticles (MNPs) present unique physico-chemical properties that make them very attractive for different biomedical applications, including magnetic hyperthermia,[1] drug delivery,[2] gene magnetofection[3] and magnetic resonance imaging (MRI).[4] In particular, iron oxide nanoparticles in the form of magnetite and maghemite are, without doubt, the most studied MNPs for clinical applications, having been used as MRI contrast agents for decades.[5] Iron oxide nanoparticles are usually classified based on their size. Superparamagnetic iron oxide nanoparticles (SPIONs) have a colloidal nanoparticle size above 50 nm and are easily sequestered by the mononuclear phagocyte system (MPS), which makes them ideal to image and diagnose liver disorders.[6] However, their short blood circulation time limits their clinical applications and some formulations have been removed from the market due to their limited scope.[7] On the other hand, ultrasmall superparamagnetic iron oxide nanoparticles (USPIONs) have longer blood half-life due to their reduced size (hydrodynamic diameter below 50 nm) and a surge of interest has emerged for the development of a new generation of MRI contrast agents based on these type of nanoparticles.[7]

MRI contrast agents are able to reduce the relaxation times of surrounding water protons under the influence of an external magnetic field. Reduction of longitudinal relaxation times, *T1*, results into positive contrast (brighter images, signal enhancement), whereas reduction of transverse relaxations times, *T2*, leads to a negative contrast (darker images, signal destruction).[8] Although both processes occur simultaneously, conventional contrast agents are classified as *T1* or *T2* depending on the relaxation time that experiences a major reduction in the presence of the contrast agent.[9] On the other hand, dual-mode contrast agents have the advantage of providing good contrast in both *T1* and *T2*-weighted images, offering unequivocal detection and facilitating the clinical diagnosis of diseases.[10] In the case of iron oxide nanoparticles, their contribution to *T1* and *T2* relaxation processes can be modulated by adjusting the nanoparticle size.[11] Accordingly, SPIONS have been traditionally used as T2 contrast enhancers, whereas smaller USPIONs with crystal sizes below 10 nm and hydrodynamic diameters under 50 nm, have shown great potential as *T1* and dual *T1/T2* contrast agents.[12–14]

Iron oxide nanoparticles are also efficient therapeutic agents used in magnetic hyperthermia. Under the influence of an alternating magnetic field (AMF), MNPs can transform magnetic energy into heat. The localized generation of heat has been exploited as a therapy for the treatment of tumors, since cancer cells are more sensitive to changes of temperature.[15] Mild hyperthermia (41-46 °C) is used to induce apoptosis in cancer cells while preserving healthy tissues. This therapy is commonly used in combination with radiation or

[a] Instituto Interuniversitario de Investigación de Reconocimiento Molecular y Desarrollo Tecnológico (IDM), Universitat Politècnica de València. Camino de Vera s/n. 46022 Valencia, Spain. E-mail: sansanca@alumni.uv.es; rmaez@qim.upv.es
[b] CIBER de Bioingeniería, Biomateriales y Nanomedicina (CIBER-BBN), Spain.
[c] Advanced (Magnetic) Theranostic Nanostructures Group, INL - International Iberian Nanotechnology Laboratory, Av. Mestre José Veiga, 4715-330 Braga, Portugal.

Electronic Supplementary Information (ESI) available. See DOI: 10.1039/x0xx00000x

chemotherapy, which results in a synergistic effect that kills cancer cells more efficiently.[16]

Combining magnetic hyperthermia and dual MRI into a single platform would therefore be especially useful for the development of new theranostic applications, *i.e.* the combination of therapy and diagnosis. However, this is a challenging undertaking because of the inherent physical limitations of magnetic nanoparticles. Large iron oxide nanoparticles present high magnetic moments, which contribute to a better heating efficiency and increased *T2*-signal enhancement. In contrast, their high magnetism impairs their performance as *T1* contrast agents due to the perturbation of *T1* relaxation processes.[11] On the other hand, *T1* relaxation is favoured in small iron oxide nanoparticles but their small size promotes energy dissipation through Néel's relaxation, limiting greatly heat production and thus any potential application for hyperthermia.[17] Accordingly, most research groups have focused on either increasing the heating efficiency and *T2* contrast of the nanoparticles or reducing their size in order to achieve better *T1* contrast. In an attempt to obtain versatile nanoparticles for both hyperthermia and dual *T1*/*T2* applications, we decided to investigate the magnetic response of USPIONs with a balanced distribution of nanoparticle sizes.

In this work, we report the preparation of USPIONs using a simple cost-effective synthetic method and evaluate their potential use for both hyperthermia and dual MRI applications. The size of the final nanoparticles was adjusted through a post-synthetic purification strategy, which led to highly-stable USPIONs with a balanced distribution of sizes centered around 10 nm. Magnetic characterization studies revealed that the nanoparticles present high saturation magnetization, being able to produce temperatures in the range of moderate hyperthermia. Interestingly, the nanoparticles also showed dual *T1/T2* signal enhancement in MRI experiments using typical clinical magnetic fields of 1.4 and 3.0 T.

Materials and methods

Reagents

$FeCl_3 \cdot 6H_2O$, $FeCl_2 \cdot 4H_2O$, oleic acid and cetyltrimethylammonium bromide (CTAB) were purchased from Sigma-Aldrich. Chloroform was purchased from Acros Organics. Ammonia (32%) and ethanol were purchased from Scharlau. 1000 ppm iron solution in nitric acid (single element solution for A.A.S.) was purchased from Fisher Chemical. Reactions were conducted using distilled water.

Nanoparticle synthesis

USPIONs composed of oleate-coated Fe_3O_4 magnetite nanocrystals were obtained by a modified coprecipitation method.[18] The reaction was conducted under argon atmosphere with mechanical stirring. In a typical procedure, 50 ml of distilled water were deoxygenated by bubbling argon through the solution. Then, temperature was increased up to 80 °C followed by the addition of 12 g of $FeCl_3 \cdot 6H_2O$ and 4.9 g of $FeCl_2 \cdot 4H_2O$. Ammonia 32% (19.53 ml) was added to the reaction mixture and iron oxide nanoparticles rapidly formed. Oleic acid (2.13 ml) was added after 30 min and the reaction was left stirring for another 90 min at 80 °C. The reaction was allowed to cool to room temperature and centrifuged at 12108 *g* (10 min) in order to precipitate the nanoparticles. Successive cycles of washing and centrifugation (12108 *g*, 10 min) were conducted using distilled water (3 cycles) and ethanol (3 cycles). The resulting black material was dried under vacuum overnight. Finally, the nanoparticles were resuspended in chloroform and centrifuged at 13400 *g* (20 min) in order to discard large aggregates and adjust the size of the final nanoparticles.

Water-phase transfer

In a typical procedure, 1 ml of oleate-coated USPIONs suspended in chloroform (6 mg/ml) was added to a 10 mg/ml solution of CTAB in water. Then, both solutions were thoroughly mixed with a probe sonicator (450 sonifier, Branson Ultrasonics Corporations) giving a homogenous oil-in-water microemulsion. The mixture was heated at 65 °C with continuous stirring until chloroform was completely evaporated, giving a clear suspension of nanoparticles in water.

Characterization techniques

Powder X-ray diffraction (PXRD) measurements were conducted using a Bruker AXS D8 Advance diffractometer equipped with CuKα radiation and working at 40 kV/40 mA. The diffraction pattern of iron oxide nanoparticles was recorded in the 2θ range between 25 and 65°.

TEM analysis was performed on a 100 kV JEOL JEM-1010 transmission electronic microscope operated with AMT image capture engine software. SAED images were obtained using a 200 kV JEM-2100F transmission electronic microscope. Samples were prepared by dropping 10 µl of nanoparticles suspended in chloroform onto carbon-coated copper grids, which were left at room temperature until chloroform was completely evaporated. The size of nanoparticles was measured using TEM analysis imaging software. SAED images were analyzed using the Digital Micrograph Software (version 3.7.4).

Dynamic light scattering (DLS) experiments were conducted with a Zetasizer Nano ZS (Malvern Instruments) equipped with a laser of 633 nm and collecting the signal at 173 °. Hydrodynamic size distributions were measured three times, from which the average PDI and Z-average values were obtained.

Fourier transform infrared spectroscopy (FTIR) was performed between 4000 and 400 cm^{-1} in absorbance mode using a Tensor 27 FTIR spectrometer (Bruker).

Thermogravimetric analysis (TGA) was conducted on a TGA/SDTA 851e balance from Mettler Toledo. The analysis was performed using a range of temperatures from 25 to 1000 °C and applying a heating rate of 10 °C/min under a flow of nitrogen.

Atomic absorption spectroscopy (AAS) measurements were conducted on a Perkin Elmer AAnalyst-100 flame atomic absorption spectrometer. Samples were prepared by digesting a 10 mg/ml water suspension of magnetic nanoparticles with nitric acid (1 M) at 55 °C for 48 h. The standard calibration curve was prepared using a 1000 ppm iron solution in nitric acid (single element solution for A.A.S.). The final iron concentration of each sample was obtained as the average value from three independent aliquots, which were digested separately.

Magnetic characterization was conducted on a Quantum Design (USA) MPMS-XL magnetometer. 50 µl of nanoparticles dispersed in chloroform were placed inside a polycarbonate capsule and sealed with vacuum grease. Field dependent magnetization was recorded at 250 K under decreasing field starting from 5 T, in the field range between -5 T and 5 T. In the temperature dependent measurements, the sample was first cooled down to 5 K in zero magnetic field (zero field cooling, ZFC). Then, a magnetic field of 10 mT was applied and the magnetic moment of the sample was measured with increasing temperature. After reaching 270 K, the magnetic moment was measured with decreasing temperature under the presence of a magnetic field of 10 mT (field cooling, FC).

Magnetic hyperthermia

Calorimetric experiments to determine the heating efficiency of the nanoparticles were conducted using a custom-made magnetic inductor that generates a stable magnetic field of 15.92 mT at 200 kHz. The magnetic field was generated inside an induction coil composed of a copper pipe, which was refrigerated using a bath circulator (Isotemp, R28 from Fisherband). The different experiments were performed at maximum power. On the centre of the inductor, the maximum field was estimated using the Biot-Savart equation:

$$B_{MAX} = \frac{i_{MAX} \cdot \mu_0 \cdot N}{2 \cdot \sqrt{r^2 + \left(\frac{l}{2}\right)^2}} \quad (1)$$

where B_{MAX} represents the maximum field, i_{MAX} the maximum current circulating in the inductor, μ_0 is the permeability of free space, N is the number of loops, l is the length of the inductor and r is the radius. The intensity current was estimated using the Ohm law, registering the voltage in the capacitor. As a result, the estimated maximum field intensity generated by the magnetic inductor was 15.92 mT.

Magnetic induction was applied inside a thermostatic chamber, which was kept at 37 °C for hyperthermia experiments. Samples were measured on disposable plastic cuvettes, which were placed inside an isolating holder at the center of the induction coil. Temperature of the samples was recorded using a fiber optic temperature sensor. The nanoparticles were also characterized using a commercial magnetic hyperthermia equipment (DM 100 system from nB nanoScale Biomagnetics).

Relaxivity measurements

Relaxation rates (R) were determined at 1.4 T using a minispec mq60 spectrometer from Bruker. Samples from 0 to 125 mM Fe were pre-heated at 37 °C and kept at this temperature during the experiments. *T1* and *T2* relaxation times were measured using standard saturation recovery and cpmg (Carr-Purcell-Meiboom-Gill) sequences respectively. The final relaxivities were obtained from the slope of the linear fit of the inverse of the relaxation times (relaxation rates) against the millimolar concentration of Fe.

MR imaging was performed in a 3.0 T horizontal bore MR Solutions Benchtop MRI system equipped with 48 G/cm actively shielded gradients. To image the samples, a 56-mm diameter quadrature birdcage coil was used in transmit/receive mode. Samples (from 0 to 100 mM Fe) were placed on a custom printed PLA wellplate (300 µL) which was then placed in the center of the scanner. Longitudinal relaxation times were measured from *T1* maps acquired using MPRAGE sequences (T_I = 12 values (0.025, 0.05, 0.075, 0.125, 0.225, 0.425, 0.825, 1.625, 3.225, 6.425, 12.825, 23.525 s), T_E = 5 ms, T_R = 24 s, A_T = 50 m 40 s), while transversal relaxation times were measured from *T2* maps acquired through MEMS sequences (T_E = 10 values (0.015 0.03 0.045 0.06 0.075 0.09 0.105 0.120.135 0.15 s), T_R = 1400 ms, N_A = 5 and A_T = 32 m 00 s). T_1 and T_2 maps were reconstructed using ImageJ software (http://imagej.nih.gov/ij). As before, the final relaxivities (*r1/r2*) were calculated from the slope of the linear fit of the relaxation rates versus the Fe concentration.

All MR images of phantoms were acquired with an image matrix 256x252, FOV 60x60 mm, 3 slices with a slice thickness of 1 mm and 0.5 mm slice gap. Image analysis was performed using ImageJ software.

Results and discussion

Nanoparticle synthesis and purification

Regarding the preparation of MNPs, Corot *et al.*[19] highlighted the importance of simple and reliable synthetic methods to obtain high-quality MNPs that do not require complex purification steps. In this work, USPIONs were prepared using a one-step reaction based on the coprecipitation of iron salts in a basic aqueous media under argon atmosphere.[18] Conducting the reaction in water facilitates the scale-up of the reaction and offers an economic and green synthetic route to produce high-quality nanoparticles for biomedical applications. Oleic acid was added to the reaction in order to control the growth of crystals and to stabilize the final nanoparticles, preventing their aggregation.[20] This is critical in order to obtain stable colloidal suspensions of monodisperse nanoparticles. Finally, the obtained nanoparticles were dispersed in chloroform in order to prevent their oxidation, giving a stable magnetic colloidal fluid or ferrofluid (see Fig. S1).

Nanoparticle characterization

The mild reaction conditions used in coprecipitation methods usually lead to nanoparticles with a broad size distribution, which is considered the main limitation of this methodology.[21]

In an attempt to separate discrete nanoparticles from aggregates and nanoparticles that were not efficiently coated, precipitation was implemented. By gradually increasing the time and speed of centrifugation, stable nanoparticles were

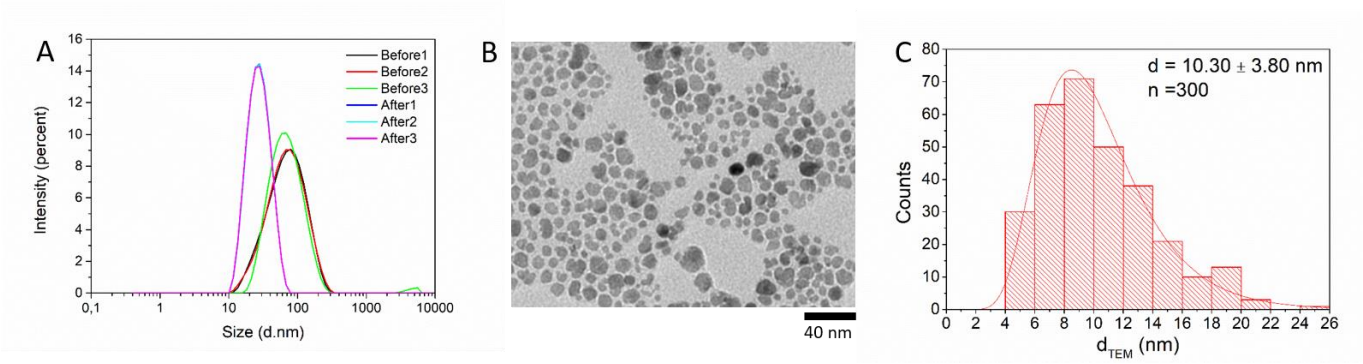

Fig. 1 Size distribution characterization. (A) Intensity-weighted nanoparticle hydrodynamic size distribution before and after the precipitation procedure. Each measurement was repeated three times. (B) Overview TEM micrograph of oleate-stabilized USPIONs after separation. (C) Size distribution of oleate-coated USPIONs after separation fitted to a log-normal distribution.

a post-synthetic purification strategy based on fractional efficiently separated from aggregates and large nanoparticles.

The size distribution of the nanoparticles during the precipitation procedure was monitored using dynamic light scattering (DLS). As can be seen in Fig. 1A, the initial ferrofluid presented a wide distribution of nanoparticle sizes, which was significantly reduced after the precipitation procedure. The polydispersity index (PDI), a dimensionless parameter used to quantify the size distribution broadness, shifted from 0.25 to 0.11 and the Z-average diameter of the nanoparticles decreased from 57.7 to 25.5 nm. With this simple and reproducible strategy, the initial wide distribution of nanoparticles was adjusted to a population with an average hydrodynamic diameter below 50 nm, the size range assigned to USPIONs.

The size and morphology of the nanoparticles were also assessed using transmission electron microscopy (TEM). The size obtained by TEM analysis refers only to the nanoparticle crystal core, in contrast to the previously obtained hydrodynamic diameter, which considers the size of the whole nanoparticle (core plus organic coating) and the diffuse double-layer of solvent molecules around it. The analysis of 300 measurements from several TEM micrographs revealed that the obtained USPIONs are formed by irregularly shaped crystals, with sizes ranging from 4 to 26 nm (Fig. 1B). This size corresponds to the measurement of the nanoparticles along their major axis, giving an average size of 10.3 ± 3.80 nm. As can be seen in Figure 1C, the nanoparticle sizes follow a log-normal distribution. This type of distribution is characteristic of magnetic nanoparticles that have been obtained through a crystal-growth mechanism, in agreement with previous observations.[22]

X-ray diffraction studies showed that the obtained USPIONs are highly crystalline, presenting sharp diffraction peaks with 2θ values of 30.21, 35.63, 43.25, 53.68, 57.28 and 62.89 (Fig. 2A). The values and relative intensities of the peaks are in agreement with the Bragg reflections of magnetite (JCPDS file no. 19-0629), which were indexed as [2 2 0], [3 1 1], [4 0 0], [4 2 2], [5 1 1] and [4 4 0].[23]

Fourier transform infrared spectroscopy (FTIR) was used to study the coating of UPSIONs with oleic acid. Oleic acid strongly interacts with the surface of iron oxide nanoparticles through the coordination of the carboxylate group to the Fe^{2+}/Fe^{3+} atoms.[24] As can be seen in Fig. 2B, the symmetric and asymmetric stretching vibration of C-H bonds in the 2800-3000 cm^{-1} region are present in the spectrum of both oleic acid and oleate-coated USPIONs but not in the uncoated nanoparticles. In the spectrum of pure oleic acid, the characteristic peak of the carboxylic C=O stretch can be found around 1700 cm^{-1}. This band is not present in the case of oleate-coated USPIONs, which exhibit two bands at 1516 and 1410 cm^{-1} that were assigned to the symmetric and asymmetric stretching of carboxylate groups, in agreement with previous studies.[25,26] This result confirms that oleic acid is effectively adsorbed on the surface of the nanoparticles as a carboxylate. Finally, the peak at 540 cm^{-1} was assigned to the Fe-O stretching vibration of the magnetite nanoparticles.

The amount of oleate adsorbed on the surface of the nanoparticles was quantified using thermogravimetric analysis (TGA). A sample of pure oleic acid was first analysed in order to determine the temperature range in which oleic acid burns. Complete degradation was observed between 150 and 600 °C, with two main losses around 260 and 360 °C (Fig. S2). TGA of the oleate-coated SPIONs showed a similar profile, with a 20.5% weight loss corresponding to the degradation of the oleate coating (Fig. 2C). No further transitions were observed above 600 °C, which indicates that the obtained iron oxide nanoparticles present good thermal stability.

Journal Name

ARTICLE

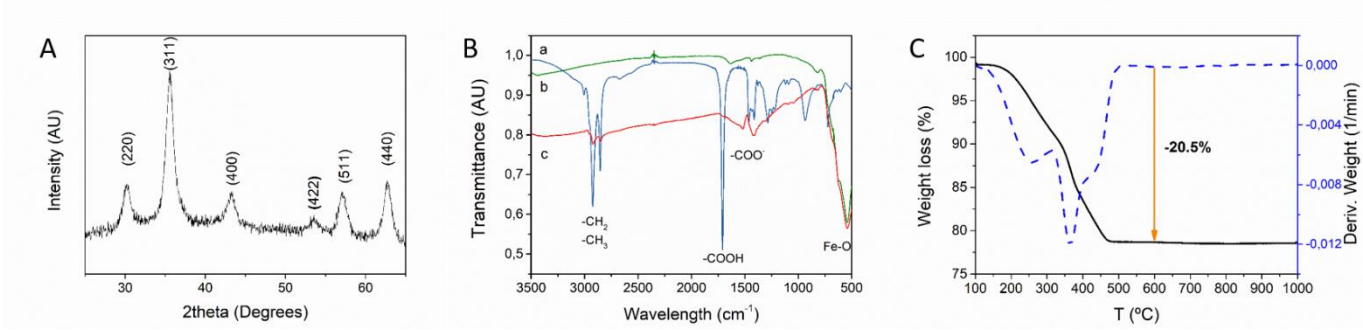

Fig. 2 Nanoparticle characterization. (A) X-ray diffraction pattern of oleate-coated USPIONs; B) FTIR spectrum of pure oleic acid (a), uncoated USPIONs (b) and oleate-coated USPIONs (c); (C) TGA and DGT of oleate-coated USPIONs.

From the TGA analysis, the amount of oleate molecules in each nanoparticle was calculated, giving a ligand density of 1635 oleate molecules/nanoparticle or 4.9 oleate molecules/nm^2 (see SI for calculations). The reported surface area occupied by the polar head of an oleate molecule is around 21 Å^2,[27] which means that nearly 5 molecules could be accommodated in a vertical position in 1 nm^2. This is the ligand density obtained for our oleate-coated USPIONs, which indicates that the surface of the nanoparticles is completely covered by a monolayer of highly-packed oleate molecules. Oleate molecules are most likely arranged in a vertical position with the carboxylate groups interacting with the surface of the nanoparticles and the hydrophobic tails exposed to the outside. Accordingly, the oleate-coated USPIONs are highly stable in non-polar organic solvents such as chloroform and hexane.

The colloidal stability of the ferrofluid, which was stored in the fridge for several months, was evaluated by DLS analysis. Measurements were taken at 6 and 8 months after the preparation of the magnetic ferrofluid, showing that the size distribution had not changed with time (Fig. S3). The absence of aggregation in the ferrofluid is an indicator of the good coverage and strong interaction of the oleate molecules with the surface of the nanoparticles. The chemical integrity of the nanoparticles was also investigated 8 months after the preparation of the ferrofluid using selected area electron diffraction (SAED). The obtained ring diffraction patterns were consistent with the crystal structure of magnetite, indicating that the nanoparticles had not experienced any significant structural modification with time (Fig. S4). All these results confirmed that the oleate-coated USPIONs are highly stable and can be stored for extended periods of time.

The hydrophobicity of the oleate-coated SPIONs is not compatible with most biomedical applications, thus a water-phase transfer was conducted in order to obtain nanoparticles stable in aqueous solutions. We employed a water-phase transfer strategy based on the use of a secondary alkylammonium salt surfactant. The hydrophobic tail of the surfactant intercalates between the oleic acid molecules through hydrophobic Van der Waals interactions, leading to the formation of a hybrid bilayer around the magnetic nanoparticles as shown in Fig. 3A.[28,29] In a typical procedure, an aqueous solution of cetyltrimethylammonium bromide (CTAB) was mixed with the ferrofluid using a probe sonicator. The resulting oil-in-water microemulsion was heated at 65 °C under continuous stirring in order to evaporate the chloroform. In contrast to the oleate-coated nanoparticles, the resulting CTAB-stabilized USPIONs are highly stable in water, as shown in Fig. 3B.

Magnetic characterization

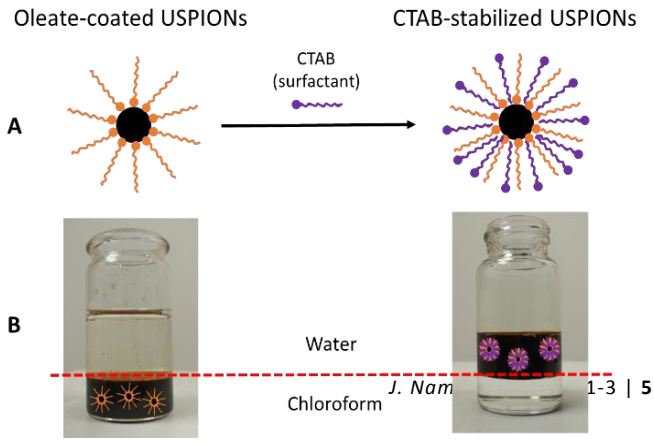

Fig. 3 (A) Interaction of CTAB with oleate molecules on the surface of USPIONs and (B) USPIONs suspended in a mixture of water-chloroform before and after the water-phase transfer.

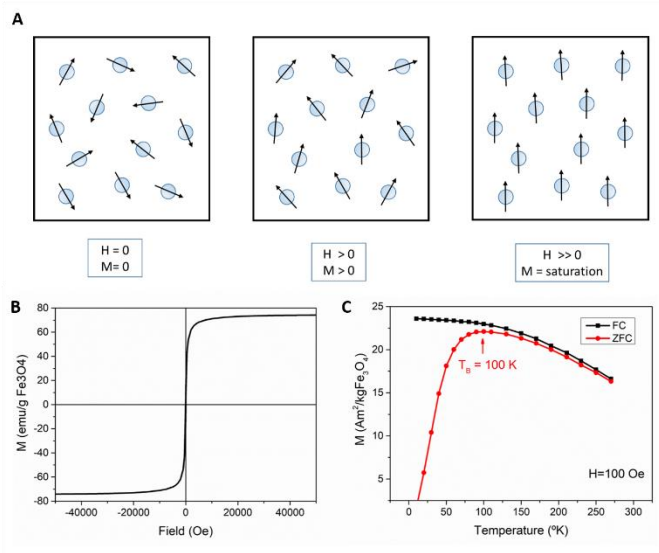

Fig. 4 (A) Alignment of individual nanoparticle magnetic moments upon the application of an external magnetic field; (B) Field-dependent magnetization curves of CTAB-stabilized USPI-ONs at 250 K and (C) ZFC/FC curves measured at 100 Oe.

It is well known that below a critical nanoparticle size, the magnetic moments of all the atoms within the nanoparticle tend to align in the same direction, forming a single magnetic domain.[30] These single-domain nanoparticles behave like small permanent magnets and therefore their magnetic moments will interact with each other and with any external magnetic field. However, if single-domain nanoparticles are small enough, their individual magnetic moments will be randomized by thermal energy, leading to a system with no net magnetization.[11] This unique phenomenon is known as superparamagnetism.[31] Thus, in the absence of an external magnetic field, the system presents no net magnetization. When an external magnetic field is applied, the individual magnetic moments of each nanoparticle align with the field and the material becomes rapidly magnetized, leading to the saturation magnetization of the material (Fig. 4A). After removal of the magnetic field, the magnetic moment of the nanoparticles return to a random distribution and the material is quickly demagnetized, a very attractive property for biomedical applications.

The magnetic properties of the obtained CTAB-stabilized USPIONs was thoroughly investigated. For field-dependent magnetization experiments, the nanoparticles were dispersed in water and kept frozen at 250 K in order to prevent nanoparticle agglomeration, which could lead to misleading results. The magnetization curves showed a small hysteresis together with negligible remanence and coercivity, confirming the superparamagnetic behaviour of the obtained nanoparticles (Fig. 4B). The nanoparticles presented high saturation magnetization (M_S=74 emu/g), close to the M_S value of bulk Fe_3O_4 (92 emu/g).[32] This reduced magnetization compared to the bulk state is commonly observed in small ferrite nanoparticles.[30,33] being generally attributed to a phenomenon known as spin canting. Spin canting was first described as a non-uniform distribution of spins, which implies that the spins of the atoms within the nanoparticle are not completely aligned.[34] This distortion of spin alignment is expected to be more pronounced at the surface of nanoparticles, leading to a higher reduction of saturation magnetization in smaller nanoparticles (high surface-to-volume-ratio).[35] However, internal structural disorder has also been suggested as a source of spin canting and cannot be excluded.[36] Additionally, it has been reported that the organic coating commonly used to stabilize iron oxide nanoparticles could have a significant influence on the magnetic properties of the resulting nanoparticles.[37] Finally, zero-field cooled/field cooled (ZFC/FC) magnetization curves revealed that the CTAB-stabilized USPIONs exhibit a superparamagnetic behaviour above 100 K (Fig. 4C).

Magnetic Hyperthermia

The generation of heat produced by single-domain magnetic nanoparticles under the influence of an alternating magnetic field (AMF) can be explained by two mechanisms: Néel and Brownian relaxation. The first process is related to the rearrangement of the spins of the atoms in the nanoparticle, which orientate towards the same direction of the external magnetic field.[38] On the other hand, the external magnetic field can induce a physical rotation of the nanoparticle itself in a process known as Brownian relaxation. Although both relaxation processes occur simultaneously, the relative contribution of each of them depends on the hydrodynamic properties of both the nanoparticles and the medium where they are dispersed.[39] The heat losses produced by these relaxation mechanisms can be determined experimentally by measuring the temperature change produced by magnetic nanoparticles under the effect of an AMF.

Calorimetric experiments were conducted using a custom-made magnetic inductor that generates a stable magnetic field of 15.92 mT at 200 kHz. The strength and frequency of the magnetic field were chosen in order to meet the criteria for safe clinical applications, in which the product H·f should be below the threshold value of 5.0×10^9 A $m^{-1}s^{-1}$.[40] A refrigerated copper induction coil was used to prevent the transfer of heat from the inductor to the sample, which was placed at the center of the coil inside an insulating holder (Fig. S5). The sample and coil were placed inside a thermostatic chamber, in which the temperature could be adjusted to simulate the body temperature and to control the initial temperature of each experiment.

Three samples (denoted as *a*, *b* and *c*) of increasing concentrations of nanoparticles (3.8, 5.7 and 7.6 mg/ml respectively) were measured in the custom-made magnetic inductor. The samples were pre-heated to 37 °C before the application of the AMF and the temperature of the liquid circulating inside the coil inductor was also set to 37 °C. The AMF was applied for 20 min to each sample, recording the increase of temperature every 10 seconds. As can be seen in Fig. 5, a steady increase of temperature was registered in all cases, indicating that the colloid suspensions are stable under the experimental conditions applied. The increase of temperature was directly proportional to the concentration of

magnetic nanoparticles, reaching temperatures within the mild hyperthermia regime. Only the sample with a higher concentration of nanoparticles (sample *c*) reached temperatures above 46 °C after 20 minutes of AMF induction. It is important to note that the concentration of nanoparticles in all the samples is below the common concentration of magnetic nanoparticles used for intratumoral injections (10 mg/ml).[41] Finally, the change of temperature in a control water sample under 20 minutes of induction was below 1 degree, which indicates that the increase of temperature is mainly produced by the magnetic nanoparticles.

The specific absorption rate (SAR, in W/g) is the preferred parameter used to measure the heating efficiency of magnetic nanoparticles and can be calculated using the following equation:[42]

$$SAR = C_f \frac{m_f}{m_{NPs}} \cdot \frac{dT}{dt} \quad (2)$$

where m_f represents the mass of the tested ferrofluid, m_{NPs} corresponds to the mass of magnetic nanoparticles and *dT/dt* represents the rate of temperature increase. C_f is the heat capacity of the ferrofluid, which can be assumed equal to that of water (4.18 J g^{-1} K^{-1}) when the amount of nanoparticles in the colloid is small compared to the amount of fluid.

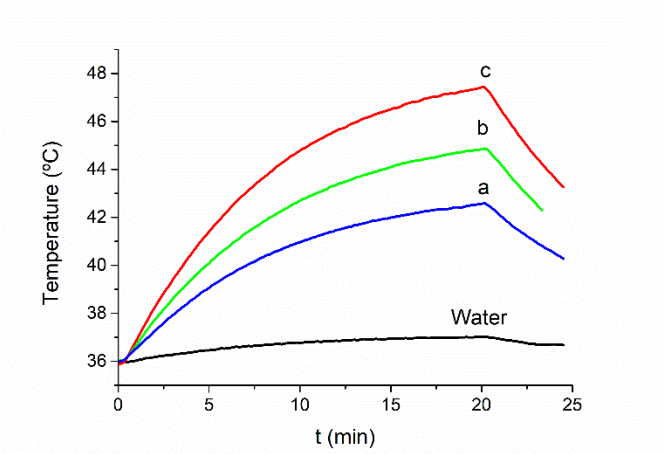

Fig. 5 Heating curves of samples *a*, *b* and *c* (3.8, 5.7 and 7.6 mg NPs/ml respectively) after 20 minutes of AMF induction (H=15.72 mT, f=200 kHz). Water was used as a control.

The heat losses of magnetic nanoparticles increase with the frequency (f) and the strength of the magnetic field (H).[43] In order to better compare the heating efficiency of magnetic nanoparticles in different experimental setups, an additional parameter known as intrinsic loss power (ILP) is commonly used:[44]

$$ILP = \frac{SAR}{f\,H^2} \quad (3)$$

SAR and ILP values of the synthesised nanoparticles were determined using equation 2 and 3. The rate of temperature increase was obtained from the heating curves at the initial time, since the temperature response is not linear in non-adiabatic systems due to heat losses to the environment.[45] For comparison purposes, the SAR and ILP values are referred to the mass of magnetite (Fe_3O_4) in each sample, which was determined using atomic absorption spectroscopy (AAS). Calculated SAR and ILP values are presented in Table 1. The obtained values for samples *a*, *b* and *c* are very similar independently of the concentration of nanoparticles, as expected for experiments conducted at the same frequency and field strength.[46] These results also indicate that the nanoparticles are highly stable under the effect of an external magnetic field, since the appearance of agglomeration would have resulted in varying SAR and ILP values.[17]

In order to validate the performance of the custom-made magnetic inductor, a forth sample (sample *d*) with a concentration of Fe_3O_4 similar to sample *a,* was measured in a commercial magnetic hyperthermia equipment. The SAR and ILP values obtained in the commercial equipment at 15 mT and 268 kHz are comparable to those obtained in the custom-made magnetic inductor, validating its applicability for hyperthermia experiments. Finally, the heating efficiency of sample *d* was evaluated using the highest field and frequency available in the commercial equipment (H= 25.2 mT and f = 835 kHz). A rapid increase of temperature was registered in the sample, which reached 70 °C within 5 minutes of AMF induction (Fig. S6). Accordingly, a significantly higher SAR value was obtained (323.22 W/g), demonstrating the great heating potential of the developed USPIONs at high fields and frequencies.

Table 1 Tested samples, experimental conditions applied (H and f) and calculated values of SAR and ILP (referred to the mass of magnetite in each sample).

Sample	a	b	c	d
[NPs] (mg/ml)	3.8	5.7	7.6	4.5
[Fe_3O_4] (mg/ml)	3.04	4.56	6.08	3.55
H (mT)	15.92	15.92	15.92	15.00
f (kHz)	200	200	200	268
SAR (W/g)	17.90	17.45	17.22	18.58
ILP (nH m^2/kg)	0.55	0.54	0.53	0.48

Relaxivity measurements

MRI contrast agents are able to reduce the longitudinal and transverse relaxation times (*T1* and *T2*) of surrounding water protons under the influence of an external magnetic field. Relaxation rates are defined as the inverse of relaxation times (*R1,2* = 1/*T1,2*), thus an effective MRI contrast agent will produce an increase of water relaxation rates. However, this effect depends on the concentration of contrast agent and an additional parameter is needed in order to compare the efficiency of different MRI contrast agents. Longitudinal and transverse relaxivities, *r*1 and *r2*, are defined as the change of water relaxation rates normalized to the concentration of contrast agent,[47] in this case the concentration of iron expressed in mM:

$$r_{1,2} = \frac{\Delta R_{1,2}}{[Fe]} \quad (4)$$

Contrast agent relaxivities are also affected by the strength of the applied magnetic field. Although the use of ultra-high field MRI (7.0 T or higher) is slowly becoming a reality for clinical applications,[48] standard clinical MRI scanners still operate at low and intermediate field strengths (from 0.5 T to 3.0 T). *T1* and *T2* water relaxation times in the presence and absence of the CTAB-stabilized USPIONs were measured using a 1.4 T relaxometer and a preclinical MRI scan working at 3.0 T. Relaxations rates (*R1* and *R2*) were plotted against the concentration of Fe, and relaxivities were obtained from the slope of the resulting curve as shown in Fig. 6A. The longitudinal and transverse relaxivites obtained at 1.4 T and 3.0 T along with the corresponding *r2/r1* ratios are presented in Table 2.

The nanoparticles presented relatively high *r2* relaxivity at the two working fields tested. The obtained *r2* values are similar, consistent with the magnetic saturation exhibited by the nanoparticles above 1.0 T (see Figure 4B). Impressively, the nanoparticles also showed a considerably high *r1* relaxivity at 1.4 T (20.5 $s^{-1}mM^{-1}$), whereas a lower value was obtained at 3.0 T (5.8 $s^{-1}mM^{-1}$). The field dependence of longitudinal relaxation is complex due to the contribution of different mechanisms,[29] but in the case of iron oxide nanoparticles a reduction of *r1* relaxivity is usually observed when the magnetic field is increased.[49,50]

Contrast agents are commonly classified based on their *r2/r1* ratio. A high *r2/r1* value indicates a dominant *T2* effect and dark contrast will be obtained in *T2*-weighted images. On the other hand, materials with a high *r1* relaxivity and a relatively low *r2/r1* (~1) will be efficient *T1* contrast agents.[51]At low fields, our USPIONs showed an intermediate *r2/r1* value of 7.7, characteristic of *T1/T2* dual contrast agents.[51,52] When the field was increased to 3.0 T, a higher *r2/r1* value was obtained due to the reduction of *r1*. However, the dual behavior of the nanoparticles was still evident, as demonstrated by the images obtained in the preclinical MRI scan (Fig. 6B). When fast spin echo (FSE) *T2*-weighted sequences were applied, a negative contrast was observed. However, upon the application of *T1*-weighted sequences, the characteristic bright contrast produced by *T1* agents was detected.

Table 2 Experimental relaxivity values obtained at 1.4 and 3.0 T, together with reported relaxivities for the commercial formulations Feraheme® and Combidex®.[21]

Sample	Field (T)	r1 ($mM^{-1}s^{-1}$)	r2 ($mM^{-1}s^{-1}$)	r2/r1
USPIONs	1.4	20.5	157	7.7
USPIONs	3.0	5.8	166	28.6
Feraheme®	1.5	15.0[a]	89[a]	5.9
Combidex®	1.5	9.9[a]	65[a]	6.6

[a]Values reported at 1.5T and 37 °C.

As shown in Table 2, *r1* and *r2* relaxivity values at 1.4 T are higher than those reported for the USPIONs formulation Combidex®, currently under clinical development in Europe for the detection of limph node metastases,[53] or the values obtained for the FDA-approved supplement Feraheme®. Interestingly, relaxivities are also higher than those reported for USPIONs synthesized using more complex high-temperature procedures,[12,54] and are even comparable to those reported for sophisticated hybrid nanodevices that combine different types of *T1* and *T2* contrast materials.[55,56] A balanced distribution of nanoparticle sizes ranging from 4 nm to 26 nm, which are log-normally distributed around 10.3 nm, might explain the good performance of the obtained USPIONs as dual *T1*/*T2* contrast agents.

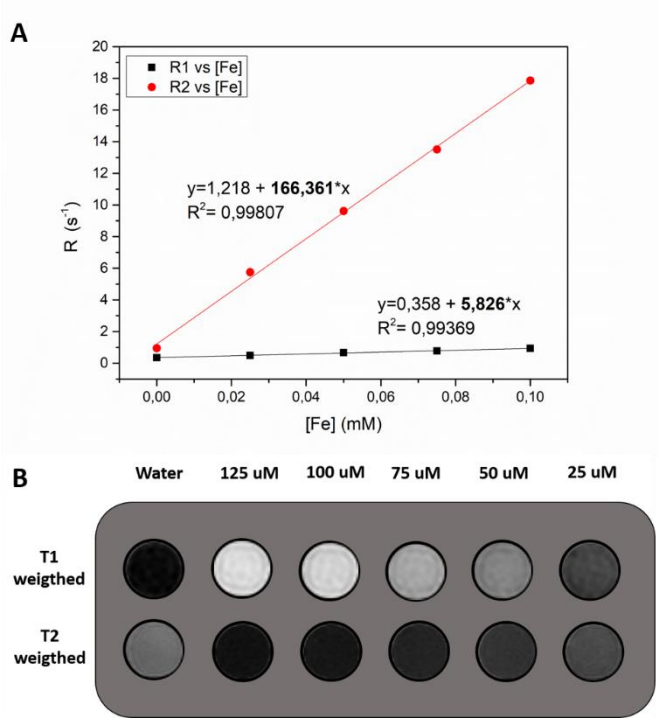

Fig. 6 (A) Dependence of longitudinal (R1) and transverse (R2) relaxation rates with the concentration of Fe. (B) T1 and T2-weighted images showing the dual behavior of CTAB-stabilized USPIONs. Measurements were conducted at 3.0 T.

Conclusions

In this work, highly-stable USPIONs were prepared through a one-step coprecipitation method. With this simple methodology, gram-scale quantities of nanoparticles were obtained using mild reaction conditions, in contrast to other sophisticated strategies that require the use of organic solvents and high reaction temperatures. The obtained nanoparticles and are coated with a highly-packed monolayer of oleate molecules, which provides increased dispersibility in organic solvents and long-term stability. The developed USPIONs are superparamagnetic at room temperature and show high saturation magnetization close to that of the bulk

material. These two features contribute to their improved heating efficiency, which proved successful in generating temperatures within the mild hyperthermia regime. The effect of the nanoparticles on water relaxation rates was also evaluated, showing *r1* and *r2* relaxivities higher than those reported for clinically used MRI contrast agents. Overall, the developed USPIONs appear as a versatile system that combines both magnetic hyperthermia and dual *T1/T2* MRI capabilities with great potential for the development of new theranostic nanodevices.

Conflicts of interest

There are no conflicts to declare.

Acknowledgements

Authors would like to acknowledge the SAI service at Universidad de Zaragoza for their support with the magnetic characterization studies. We also thank the assistance of the Electron Microscopy Service at UPV. We are grateful to the Spanish Government (projects MAT2015-64139-C4-1-R and AGL2015-70235-C2-2-R (MINECO/FEDER)) and the Generalitat Valenciana (Projects PROMETEO/2018/024 and PROMETEOII/2014/047) for financial support. S.S.C. is grateful to the Spanish MEC for his FPU grant.

References

1 J.-H. Lee, J. Jang, J. Choi, S. H. Moon, S. Noh, J. Kim, J.-G. Kim, I.-S. Kim, K. I. Park and J. Cheon, *Nat. Nanotechnol.*, 2011, **6**, 418–422.

2 A. K. Hauser, R. J. Wydra, N. A. Stocke, W. Anderson and J. Z. Hilt, *J. Control. Release*, 2015, **219**, 76–94.

3 J. M. Chem, B. Gonz, E. Ruiz-Hernández, C. Ram and T. Portol, *J. Mater. Chem.*, 2011, **21**, 4598–4604.

4 J. Gallo, N. J. Long and E. O. Aboagye, *Chem. Soc. Rev.*, 2013, **42**, 7816–33.

5 C. Boyer, M. R. Whittaker, V. Bulmus, J. Liu and T. P. Davis, *NPG Asia Mater.*, 2010, **2**, 23–30.

6 Y.-X. J. Wang, *Quant. Imaging Med. Surg.*, 2011, **1**, 35–40.

7 Y. X. J. Wáng and J.-M. Idée, *Quant. Imaging Med. Surg.*, 2017, **7**, 88–122.

8 C. Blanco-Andujar, A. Walter, G. Cotin, C. Bordeianu, D. Mertz, D. Felder-Flesch and S. Begin-Colin, *Nanomedicine*, 2016, **11**, 1889–1910.

9 T. Shin, Y. Choi, S. Kim and J. Cheon, *Chem. Soc. Rev.*, 2015, **44**, 4501–4516.

10 M. A. Busquets, J. Estelrich and M. J. Sánchez-Martín, *Int. J. Nanomedicine*, 2015, **10**, 1727–1741.

11 N. Lee and T. Hyeon, *Chem. Soc. Rev.*, 2012, **41**, 2575–2589.

12 G. Wang, X. Zhang, A. Skallberg, Y. Liu, Z. Hu, X. Mei and K. Uvdal, *Nanoscale*, 2014, **6**, 2953.

13 B. H. Kim, N. Lee, H. Kim, K. An, Y. Il Park, Y. Choi, K. Shin, Y. Lee, S. G. Kwon, H. Bin Na, J. G. Park, T. Y. Ahn, Y. W. Kim, W. K. Moon, S. H. Choi and T. Hyeon, *J. Am. Chem. Soc.*, 2011, **133**, 12624–12631.

14 A. H. Negussie, P. S. Yarmolenko, A. Partanen, A. Ranjan, G. Jacobs, D. Woods, H. Bryant, D. Thomasson, M. W. Dewhirst, B. J. Wood and M. R. Dreher, *Int. J. Hyperthermia*, 2011, **27**, 140–55.

15 A. Hervault and N. Thi Kim Thanh, *Nanoscale*, 2014, **6**, 11553–11573.

16 C. S. S. R. Kumar and F. Mohammad, *Adv. Drug Deliv. Rev.*, 2011, **63**, 789–808.

17 A. E. Deatsch and B. a. Evans, *J. Magn. Magn. Mater.*, 2014, **354**, 163–172.

18 J. Zhang, X. Li, J. M. Rosenholm and H. Gu, *J. Colloid Interface Sci.*, 2011, **361**, 16–24.

19 C. Corot, P. Robert, J. M. Idée and M. Port, *Adv. Drug Deliv. Rev.*, 2006, **58**, 1471–1504.

20 M. Gonzales, L. M. Mitsumori, J. V. Kushleika, M. E. Rosenfeld and K. M. Krishnan, *Contrast Media Mol. Imaging*, 2010, **5**, 286–293.

21 S. Laurent, D. Forge, M. Port, A. Roch, C. Robic, L. Vander Elst and R. N. Muller, *Chem. Rev.*, 2008, **108**, 2064–110.

22 L. B. Kiss, J. Söderlund, G. A. Niklasson and C. G. Granqvist, *Nanotechnology*, 1999, **10**, 25–28.

23 H. E. Swanson, H. F. McMurdie, M. C. Morris and E. H. Evans, *Natl. Bur. Stand.*, 1967, **25**, 31.

24 R. De Palma, S. Peeters, M. J. Van Bael, H. Van Den Rul, K. Bonroy, W. Laureyn, J. Mullens, G. Borghs and G. Maes, *Chem. Mater.*, 2007, **19**, 1821–1831.

25 P. Roonasi and A. Holmgren, *Appl. Surf. Sci.*, 2009, **255**, 5891–5895.

26 K. Yan, H. Li, X. Wang, C. Yi, Q. Zhang, Z. Xu, H. Xu and A. K. Whittaker, *J. Mater. Chem. B*, 2014, **2**, 546–555.

27 E. R. Garland, E. P. Rosen, L. I. Clarke and T. Baer, *Phys. Chem. Chem. Phys.*, 2008, **10**, 3156.

28 H. Fan, K. Yang, D. M. Boye, T. Sigmon, K. J. Malloy, H. Xu, G. P. López and C. J. Brinker, *Sci. Reports*, 2004, **304**, 567–571.

29 E. D. Smolensky, H. Y. E. Park, Y. Zhou, G. A. Rolla, M. Marjańska, M. Botta and V. C. Pierre, *J. Mater. Chem. B*, 2013, **1**, 2818–2828.

30 R. H. Kodama, *J. Magn. Magn. Mater.*, 1999, **200**, 359–372.

31 C. P. Bean and J. D. Livingston, *J. Appl. Phys.*, 1959, **30**, S120–S129.

32 Q. Li, C. W. Kartikowati, S. Horie, T. Ogi, T. Iwaki and K. Okuyama, *Sci. Rep.*, 2017, **7**, 9894.

33 A. G. Roca, M. P. Morales, K. O'Grady and C. J. Serna, *Nanotechnology*, 2006, **17**, 2783–2788.

34 J. M. D. Coey, *Phys. Rev. Lett.*, 1971, **27**, 1140–1142.

35 S. Linderoth, P. V. Hendriksen, F. Bødker, S. Wells, K. Davies, S. W. Charles and S. Mørup, *J. Appl. Phys.*, 1994, **75**, 6583–6585.

36 C. J. Serna, F. Bùdker, S. Mùrup, M. P. Morales, F. Sandiumenge and S. Veintemillas-Verdaguer, *Solid State Commun.*, 2001, **118**, 437–440.

37 T. J. Daou, J. M. Grenèche, G. Pourroy, S. Buathong, A. Derory, C. Ulhaq-Bouillet, B. Donnio, D. Guillon and S. Begin-Colin, *Chem. Mater.*, 2008, **20**, 5869–5875.

38 S. Laurent, S. Dutz, U. O. Häfeli and M. Mahmoudi, *Adv. Colloid Interface Sci.*, 2011, **166**, 8–23.

39 N. T. Thanh, *Magnetic Nanoparticles From Fabrication to Clinical Applications*, CRC Press, Boca Raton, 2012.

40 R. Hergt and S. Dutz, *J. Magn. Magn. Mater.*, 2007, **311**, 187–192.

41 R. Hergt, S. Dutz, R. Müller and M. Zeisberger, *J. Phys. Condens. Matter*, 2006, **18**, S2919–S2934.

42 D.-H. K. D.-H. Kim, Y. T. Thai, D. E. Nikles and C. S. Brazel, *IEEE Trans. Magn.*, 2009, **45**, 64–70.

43 R. E. E. Rosensweig, *J. Magn. Magn. Mater.*, 2002, **252**, 370–374.

44 D. Ortega and Q. A. Pankhurst, in *Nanoscience: Volume 1: Nanostructures through Chemistry*, ed. P. O'Brien, The Royal Society of Chemistry, Cambridge, 2013, vol. 1, pp. 60–88.

45 R. R. Wildeboer, P. Southern and Q. A. Pankhurst, *J. Phys. D. Appl. Phys.*, 2014, **47**, 495003.

46 C. Guibert, V. Dupuis, V. Peyre and J. Fresnais, *J. Phys. Chem. C*, 2015, **119**, 28148–28154.

47 C. Henoumont, S. Laurent and L. Vander Elst, *Contrast Media Mol. Imaging*, 2009, **4**, 312–321.

48 T. N. Parac-Vogt, S. Biju, J. Gallo, M. Bañobre-López, B. Manshian, S. Soenen, U. Himmelreich and L. Vander Elst, *Chem. Eur. J.*, 2018, **24**, 7388–7397.

49 M. Rohrer, H. Bauer, J. Mintorovitch, M. Requardt and H. J. Weinmann, *Invest. Radiol.*, 2005, **40**, 715–724.

50 Y. Gossuin, P. Gillis, A. Hocq, Q. L. Vuong and A. Roch, *Wiley Interdiscip. Rev. Nanomedicine Nanobiotechnology*, 2009, **1**, 299–310.

51 N. Guldris, B. Argibay, Y. V. Kolen'ko, E. Carbó-Argibay, T. Sobrino, F. Campos, L. M. Salonen, M. Bañobre-López, J. Castillo and J. Rivas, *J. Colloid Interface Sci.*, 2016, **472**, 229–236.

52 F. Hu and Y. S. Zhao, *Nanoscale*, 2012, **4**, 6235–43.

53 H. E. Daldrup-Link, *Radiology*, 2017, **284**, 616–629.

54 F. Hu, Q. Jia, Y. Li and M. Gao, *Nanotechnology*, 2011, **22**, 245604.

55 T. Tegafaw, W. Xu, M. W. Ahmad, J. S. Baeck, Y. Chang, J. E. Bae, K. S. Chae, T. J. Kim and G. H. Lee, *Nanotechnology*, 2015, **26**, 365102.

56 G. H. Im, S. M. Kim, D. G. Lee, W. J. Lee, J. H. Lee and I. S. Lee, *Biomaterials*, 2013, **34**, 2069–2076.